JOURNAL OF GEOPHYSICAL RESEARCH, VOL. 96, NO. C8, PAGES 14,979–14,993, AUGUST 15, 1991

Dynamics of the Coastal Transition Zone Jet
1. Linear Stability Analysis

STEPHEN D. PIERCE, J. S. ALLEN, AND LEONARD J. WALSTAD

College of Oceanography, Oregon State University, Corvallis

The linear stability of a coastal transition zone (CTZ) jet is analyzed using a six-layer quasi-geostrophic model with observed basic state velocity profiles. The velocity profiles are obtained from objectively analyzed hydrographic and acoustic doppler data from the 1987 CTZ pilot experiment. Along-jet perturbation wavelengths of 260-265 km are found to be the most unstable, with *e*-folding growth periods of 7-11 days and along-jet phase speeds of 4-8 km/d downstream. Energy transformation terms and energy budgets are discussed. Both barotropic and baroclinic instability processes are important.

1. INTRODUCTION

The dynamics of the transition zones between open ocean and upwelling regions along eastern ocean boundaries are not well understood. The northern California example of a coastal transition zone (CTZ), with its intriguing filaments or jets, has recently been the subject of a major observational effort [*CTZ Group*, 1988]. In the late spring and summer of 1987, two hydrographic and shipboard acoustic doppler current profiler (ADCP) surveys revealed an intense equatorward jet along the boundary between cool and saline upwelled water and warmer, fresher offshore water [*Kosro et al.*, this issue]. The presence of this mesoscale jet with energetic meanders anywhere from 100 to 400 km in size is by now an expected feature of this region and season [*Strub et al.*, this issue; *Huyer et al.*, this issue]. Some of the dynamical questions suggested by these observations involve the nature and structure of these jet meanders. Why does a meander grow? What determines its wavelength? If the growth can be explained as an instability, what source of energy feeds the instability? These questions may be approached in a variety of ways.

Walstad et al. [this issue] take advantage of the combination of hydrographic and ADCP data from the 1987 experiment to perform quasi-geostrophic data assimilation studies. Initial conditions are specified by objective analysis of the May 22 data set. The model is time-stepped forward to June 12 using boundary conditions obtained by linear interpolation between the May 22 and June 12 observations. The four-dimensional field estimate of the flow is obtained by varying the objective analysis parameters until the final June 12 quasi-geostrophic solution is in best agreement with the observed June 12 field. The agreement is fairly good (see *Walstad et al.* [this issue] for details). The structure and energetics of the solution are then analyzed.

The present study (part 1) regards a jet meander as a possible linear instability of a quasi-geostrophic basic state flow. We consider two-dimensional velocity sections of the jet extracted from the objectively analyzed May 22 and June 12, 1987, data sets as the basic states for the stability analyses. The formulation allows for both barotropic and baroclinic instability processes. We obtain phase speeds, growth rates, and modal structure of the perturbations as a function of along-jet wavelength. In addition, we examine the transformation of kinetic and potential energy to the perturbations, presenting integrated energy budgets and maps of the relevant terms in the quasi-geostrophic energy balance.

In part 2, *Allen et al.* [this issue] continue the stability study by examining the nonlinear, finite amplitude behavior of the CTZ jet. One of the basic state profiles we analyze here in part 1 is used as an initial condition for a time-dependent, nonlinear quasi-geostrophic model in a periodic f plane channel. The jet structure is perturbed and the evolution of the stream function, vertical velocity, vorticity, and potential vorticity fields is examined. Some of the results presented in part 2 use the most unstable linear mode found in part 1 to perturb the nonlinear model. The contributions of different terms to the kinetic and potential energy balances are also assessed in part 2.

Although the literature involving studies of the stability of mean flows is extensive, historically the majority of it concentrates on one-dimensional cases, i.e., either pure baroclinic or pure barotropic instabilities. This is not surprising since the two-dimensional case is difficult analytically [*Pedlosky*, 1987, section 7.15]; the normal-mode equation is nonseparable. With increasing computer capabilities, however, numerical solutions have become viable. Important idealized studies of the mixed stability problem include *Hart* [1974] and *Holland and Haidvogel* [1980], which each explore parameter space using specific two-layer idealized mean state profiles. *Killworth* [1980] offers a less in-depth but broader overview of the mixed stability of many different idealized profiles. The present work in some ways builds upon *Haidvogel and Holland* [1978], who analyze the mixed stability of profiles obtained from general circulation model output; we extend their two-layer model to an arbitrary number of layers (six for our standard case).

The emphasis of the present study is on the use of specific observed basic state profiles to produce results relevant to the CTZ region. Although *Johns* [1988] does not treat the mixed stability case, his pure baroclinic study of Gulf Stream meanders using actual data is similar to our approach. *Beckmann* [1988], who treats the mixed instability case for jet modes in the eastern North Atlantic, also uses methods similar to the present study.

2. OBSERVED JET

Kosro et al. [this issue] provide a complete description of the late spring and summer (May 18-27 and June 9-19) 1987 surveys; only a brief overview of the data relevant to this study is given here. The nominal station grid for the surveys consists of two alongshore lines about 90 and 150 km from the coast, connected by four cross-shore lines to form three subgrids with approximately 15-km station spacing. Hydrographic data to at least 495

Paper number 91JC00979.
0148-0227/91/91JC-00979$05.00

m depth were collected at 76 stations for each survey, and good quality acoustic doppler current profiler (ADCP) data were collected continuously along the shiptrack.

ADCP data at 121 m are used by *Walstad et al.* [this issue] to reference the hydrographic measurements, thus determining the absolute geostrophic flow field for the upper 500 m along the station grid. We utilize the objective analysis of this combined data set as presented by *Walstad et al.* [this issue]. This method includes extrapolation of both the density and the velocity fields below 500 m using historical data and the first baroclinic mode. For each of the surveys, the correlation function for the objective analysis is assumed independent of time and an estimate of the density and velocity fields is made for the midpoint of the cruise: May 22 and June 12. The reader is referred to *Walstad et al.* [this issue] for the details and approximations inherent in these techniques. Examples of the resulting stream function fields, at 50 m depth, are shown in Figure 1.

For the purpose of our stability analysis, we extract one two-dimensional vertical section of the flow field from each survey and use this as our basic state. The locations of these sections (Figure 1) are chosen subjectively, with an eye toward catching the jet where it is least affected by other phenomena such as eddies. Ideally, we want to choose a place where the jet does not seem to be part of a mature meander. It is debatable within linear stability theory whether it is more appropriate to use "snapshots" such as these or some type of observational mean for the basic state profiles. Although some sort of average might seem more relevant than a local calculation at one point in the jet, this average will not necessarily be related to the theoretical unperturbed form of the flow. As discussed by *Pedlosky* [1987, section 7.1], any real time average will be affected by the very perturbations which we seek to study. Our choice is to make a best guess at the structure of a fluctuation-free jet and to use this as our "mean" state. The paradigm of this flow field as a mean jet plus a perturbation seems justified aposteriori by nonlinear results from part 2, which reveal a jet retaining much the same form as the unperturbed flow even through the course of large meanders.

We examine the stability of the observed jet profiles over a flat bottom, without complicating effects from bottom topography. Although the CTZ region is located adjacent to the continental slope, where bottom topography may affect the dynamics, observations of the jet location during 1987 indicate that the core of the jet was mostly found offshore of the continental slope [*Kosro et al.*, this issue]. Within the analysis region used by *Walstad et al.* [this issue], the northeastern corner of the grid does include a narrow strip of the outer continental slope region. Yet the remainder of the region does not contain substantial topography. Since the time-dependent jet is constantly altering its orientation with respect to the local bottom topography, it is difficult to specify an appropriate mean relative position. In addition, recall that we do not have CTZ observations available below 500 m depth. The stream function values below this point are obtained using extrapolation and available historical data and are consequently not well determined. We feel that these uncertainties preclude the specification of bottom topography in a meaningful manner. Thus we assume a flat bottom for this initial analysis.

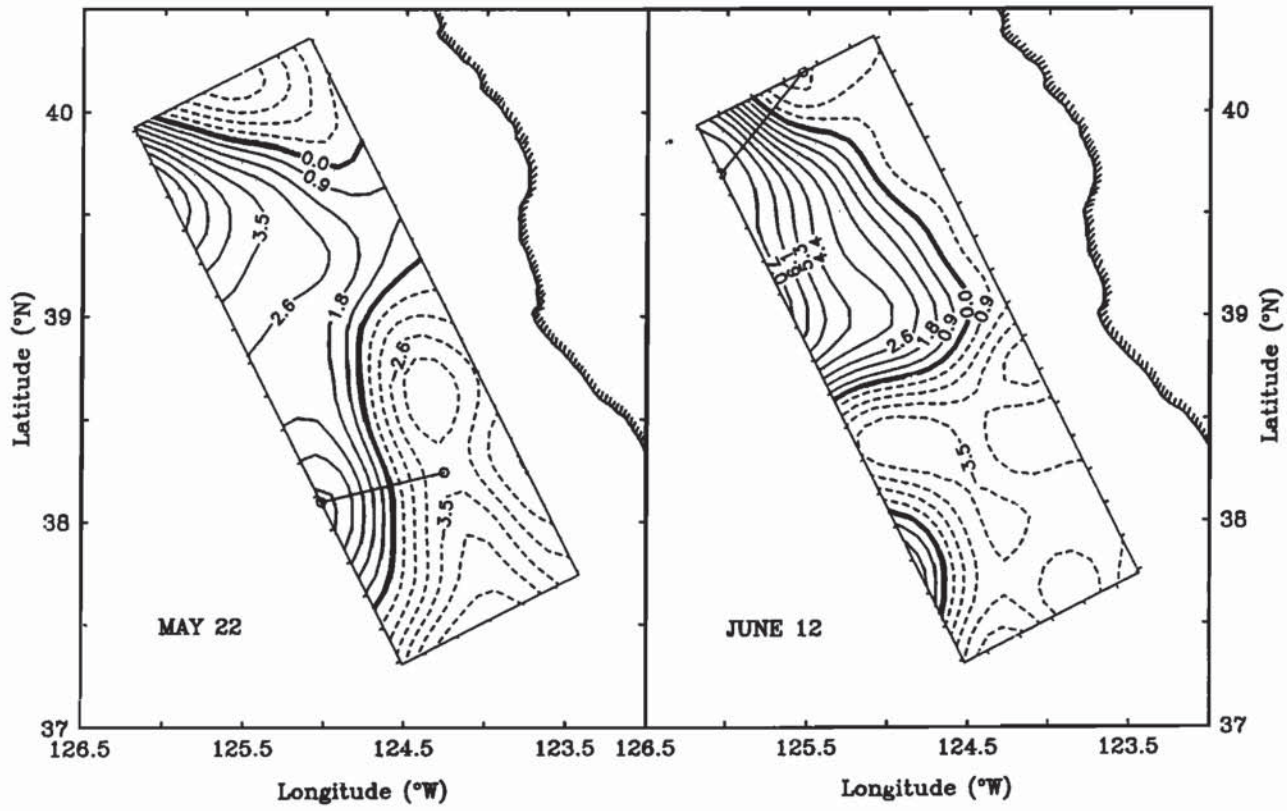

Fig. 1. Stream function at 50 m from objective analysis of combined hydrographic and ADCP data from the late spring and summer 1987 surveys [*Walstad et al.*, this issue]. The contour interval is equivalent to 2 dynamic cm. The two lines drawn between small circles indicate locations of the vertical sections extracted for the stability analyses.

3. LINEAR STABILITY MODEL

Formulation

The linear stability model follows the development by *Haidvogel and Holland* [1978] extended to an arbitrary number of layers. Consider a quasi-geostrophic model with N layers of constant density ρ_n and undisturbed layer thicknesses H_n, where $n = 1, 2, \ldots, N$ ($n = 1$ is the surface layer). The subscript $n + 1/2$ denotes a variable defined at the interface between layers n above and $n+1$ below. The stream function for each layer is $\psi_n = \psi_n(x, y, t)$ and the geostrophic velocity components are

$$u_n = -\psi_{ny}, \quad v_n = \psi_{nx}, \tag{1}$$

where (x, y) are Cartesian coordinates, t is time, and subscripts (x, y, t) denote partial differentiation. Consider the inviscid quasi-geostrophic vorticity and density equations, on an f plane, in terms of the stream function ψ_n for layers $n = 1, N$:

$$\nabla^2\psi_{nt} + J(\psi_n, \nabla^2\psi_n) + f_0 H_n^{-1}(w_{n+1/2} - w_{n-1/2}) = 0, \tag{2}$$

$$(\psi_n - \psi_{n+1})_t = J(\psi_n - \psi_{n+1}, \psi_{n+1/2}) - g'_{n+1/2} f_0^{-1} w_{n+1/2}, \tag{3}$$

where $$\psi_{n+1/2} = \frac{H_{n+1}}{H_n + H_{n+1}}\psi_n + \frac{H_n}{H_n + H_{n+1}}\psi_{n+1}, \tag{4}$$

and H_n is layer thickness (total depth $H = H_1 + H_2 + \cdots H_N$), $g'_{n+1/2} = g(\rho_{n+1} - \rho_n)/\rho_0$ is reduced gravity, f_0 is the Coriolis parameter, and J is the Jacobian operator. Vertical boundary conditions are $w_{1/2} = w_{N+1/2} = 0$ at $z = 0, -H$.

Combine (2) and (3) to form equations for potential vorticity conservation: for the top layer,

$$\frac{D_1}{Dt}\{\nabla^2\psi_1 + \frac{H}{H_1}F_1[\psi_2 - \psi_1]\} = 0, \tag{5a}$$

for $n = 2, (N-1)$,

$$\frac{D_n}{Dt}\{\nabla^2\psi_n + \frac{H}{H_n}[F_n(\psi_{n+1} - \psi_n) - F_{n-1}(\psi_n - \psi_{n-1})]\} = 0, \tag{5b}$$

and for the bottom layer,

$$\frac{D_N}{Dt}\{\nabla^2\psi_N - \frac{H}{H_N}F_{N-1}[\psi_N - \psi_{N-1}]\} = 0, \tag{5c}$$

where $F_n = f_0^2/g'_{n+1/2}H$ and $\frac{D_n}{Dt} = \frac{\partial}{\partial t} + u_n\frac{\partial}{\partial x} + v_n\frac{\partial}{\partial y}$.

To simplify the stability problem to a tractable one, we assume that the basic state flow is two-dimensional and independent of time. Consider a channel of width L with coordinates (x, y) along-channel and cross-channel, respectively, and ψ_n as the basic mean state $\Psi_n(y)$ plus a small perturbation $\gamma\phi_n(x, y, t)$, i.e. $\psi_n = \Psi_n(y) + \gamma\phi_n(x, y, t)$, where $\gamma \ll 1$. Linearize (5b) about the basic state in the usual way:

$$(\frac{\partial}{\partial t} + U_n\frac{\partial}{\partial x})\{\nabla^2\phi_n + \frac{H}{H_n}[F_n(\phi_{n+1} - \phi_n) - F_{n-1}(\phi_n - \phi_{n-1})]\}$$

$$-\phi_{nx}\{U_{nyy} + \frac{H}{H_n}[F_n(U_{n+1} - U_n) - F_{n-1}(U_n - U_{n-1})]\} = 0, \tag{6}$$

where $U_n = -\Psi_{ny}$. Equations (5a) and (5c) are linearized in similar fashion. In subsequent equations, the range of $n = 1, N$ and the simplified formulations for the $n = 1$ and $n = N$ cases will be implicit.

We consider solutions to (6) of the form

$$\phi_n = \mathrm{Re}[\hat{\phi}_n(y)e^{ik(x-ct)}], \tag{7}$$

where the wavenumber k is taken to be real, but c and $\hat{\phi}_n$ are complex. Substitution into (6) yields

$$(U_n - c)\{\hat{\phi}_{nyy} - k^2\hat{\phi}_n + \frac{H}{H_n}[F_n(\hat{\phi}_{n+1} - \hat{\phi}_n) - F_{n-1}(\hat{\phi}_n - \hat{\phi}_{n-1})]\}$$

$$-\hat{\phi}_n\{U_{nyy} + \frac{H}{H_n}[F_n(U_{n+1} - U_n) - F_{n-1}(U_n - U_{n-1})]\} = 0. \tag{8}$$

For the domain $0 < y < L$, the boundary conditions for (8) are $\hat{\phi}_n(0) = \hat{\phi}_n(L) = 0$, forming an eigenvalue problem for $\hat{\phi}_n$ with eigenvalue c. For $c = c_r + ic_i$, solutions with $c_i > 0$ indicate temporal instability with exponential growth rate kc_i.

Using a centered second-order finite difference approximation in y, we solve the above problem numerically. Defining $\hat{\phi}_{n,j}$ as $\hat{\phi}$ of the nth layer at the jth grid point in y, we form the generalized complex eigenvalue problem,

$$c\mathbf{A}\bar{\phi} = \mathbf{B}\bar{\phi}, \tag{9}$$

where $\bar{\phi}$ is the eigenvector composed of $\hat{\phi}_{n=1,N;\,j=1,M}$ and $\mathbf{A}$ and $\mathbf{B}$ are $NM \times NM$ matrices of coefficients. Equation (9) can be solved using an algorithm by *Kaufman* [1975], or a slightly modified IMSL version (routine *gvccg*). For a given basic state flow, we seek solutions for the eigenvalue c and eigenvector structure $\hat{\phi}$ over a range of wavenumbers k. The algorithm was verified through reproduction of stability results from *Killworth* [1980] and *Holland and Haidvogel* [1980].

Walstad et al. [this issue] choose a six-layer scheme to resolve the vertical; we use the same for consistency, although we later investigate the effect of increasing the number of layers (see section 6). Both the May 22 and June 12 standard six-layer basic states use the same values for layer depths and reduced gravities (Table 1 and Figure 2). The model N^2 profile is also shown (Figure 2*a*), $N^2 = g'_{n+1/2}/(z_n - z_{n+1})$, where z_n is the mid-depth of layer n. The two basic states in Figure 2 are similar, although the June 12 jet is more intense than the May 22 one, with maximum speeds ≈ 0.9 m s^{-1} rather than ≈ 0.5 m s^{-1}. The two cases provide a useful range within which most examples of a jet would probably lie. We concentrate on the results from the May 22 case since the smaller values of horizontal and vertical shear are less likely to give overestimates of instability processes for the jet in general.

Local Rossby numbers U_y/f calculated across the jet reach maximums of about 0.2; this is within the range where quasi-geostrophic dynamics remains a useful approximation. The first baroclinic Rossby radius of deformation calculated from the six-layer observed jet is $R_d = 24.6$ km. To estimate cross-jet length scales, we fit a Gaussian analytical form $U = U_0\exp(-y^2/L^2)$ to

TABLE 1. Six-Layer Basic State Characteristics

Layer	Thickness, m	$g\Delta\rho/\rho_0$, m s^{-2}
1 (surface)	100	
		1.0655×10^{-2}
2	100	
		3.3704×10^{-3}
3	100	
		3.6904×10^{-3}
4	400	
		4.6926×10^{-3}
5	800	
		3.9488×10^{-3}
6 (bottom)	1672	

The Rossby radius for the first baroclinic mode, $R_d = 24.6$ km.

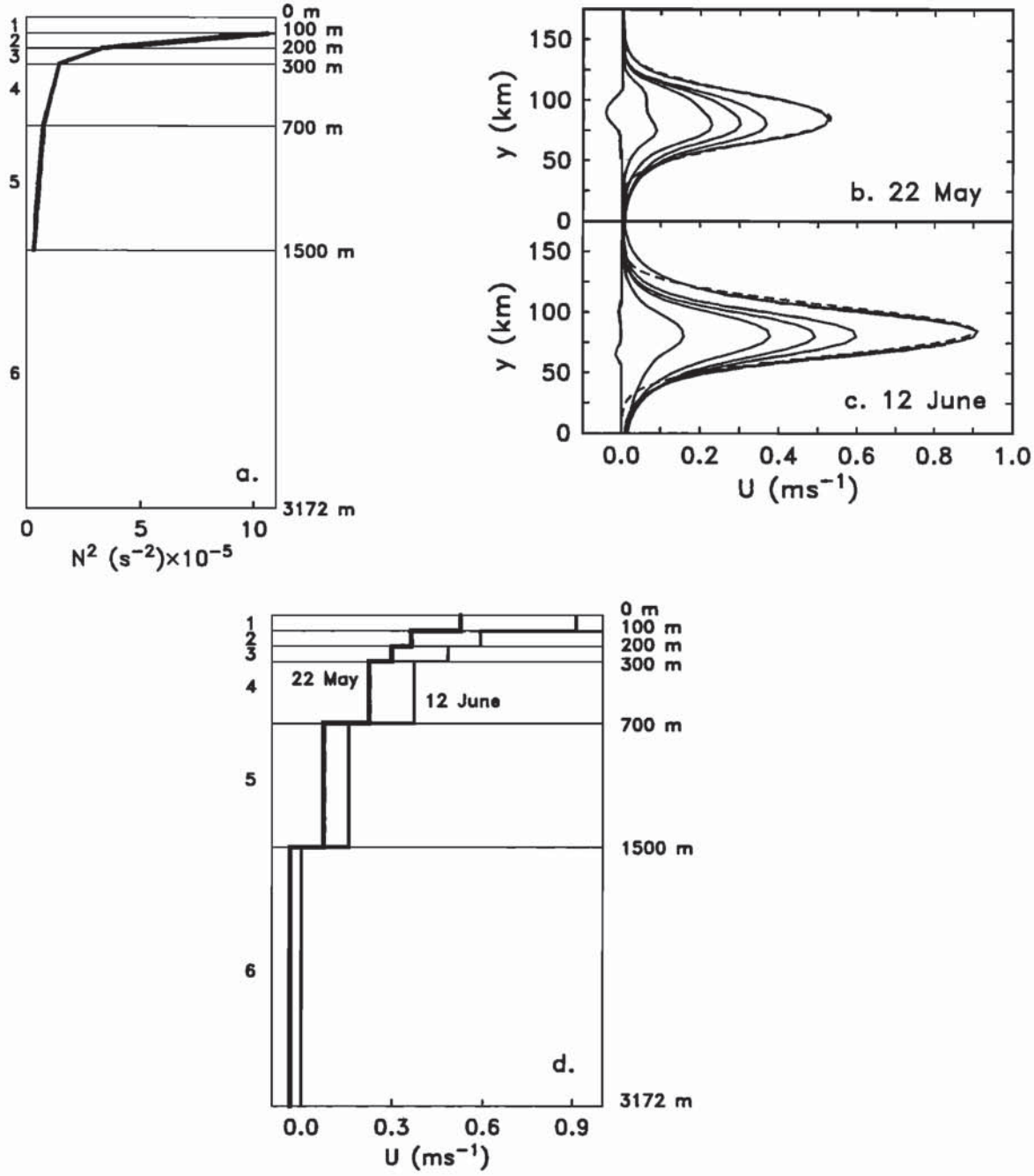

Fig. 2. Standard six-layer basic state profiles: (*a*) layer thicknesses and N^2 profile, which are the same for both cases; (*b*) May 22 and (*c*) June 12 velocity profiles versus cross-jet distance *y* for layers 1-6; and (*d*) velocity profiles vs. depth at the core of the jet ($y=85$ km). The dashed lines which nearly coincide with the layer 1 profiles in Figures 2*b* and 2*c* are Gaussian fits to the horizontal jet. These are examples of the fits used to estimate a cross-jet length scale (half width) of $L=29\pm1$ km.

the horizontal profiles (Figures 2*b* and 2*c*, dashed lines) and obtain an estimate of $L=29\pm1$ km (half width). Since the ratio $R_d/L \sim O(1)$, parameter studies such as *Killworth* [1980] predict the possibility of mixed instability.

The linear stability analysis uses 175 km for the model channel width. Figures 2, 12, and 14 indicate this 175-km-wide channel. Figures 6-9 show a jet centered within a wider 350-km region. The wider channel is shown for clarity and for consistency with the presentation of some of the finite amplitude results of part 2; all of our results in part 1 are calculated using a 175-km channel width. Model grid spacing across the channel is 5 km, resulting in 36 grid points in the across-channel coordinate *y*. The tails of the velocity profiles (10-15 km in length) at the *y* boundaries were smoothed exponentially to zero. Experimentation with doubling the horizontal resolution in *y* did not change the results substantially; results for the maximum growth rate of the fluctuation were within 1% of the basic case. We also investigated the effects of using a full 350-km-wide channel for selected cases, and the results were not qualitatively different. As expected [e.g., *Beckmann*, 1988], the increased cross-jet scale allowed for slightly

(≈5%) larger growth rates. For simplicity and computational efficiency, we retain our choice of the 175-km-wide region.

Energetics

The energetics governing the growth of a perturbation in a current with both vertical and horizontal shear, as in the present case, are especially interesting. The energy transformations of both barotropic and baroclinic instability processes are occurring simultaneously; even the signs of the energy terms will be uncertain a priori, as discussed by *Pedlosky* [1987, section 7.15].

We derive the quasi-geostrophic kinetic energy balance for the perturbations by multiplying (6) by $-\phi_n H_n$ and rearranging terms to yield

$$\frac{1}{2} H_n(\nabla\phi_n \cdot \nabla\phi_n)_t = H_n\nabla\cdot(\phi_n\nabla\phi_{nt}) + H_n\Psi_{ny}\frac{1}{2}(\nabla\phi_n\cdot\nabla\phi_n)_x - H_n\phi_{nx}\phi_{ny}\Psi_{nyy} + H_n\nabla\cdot[-\phi_n\Psi_{ny}(\nabla\phi_n)_x + \phi_n\phi_{nx}\Psi_{nyy}\hat{j}] - f_0 w_{n-1/2}\phi_{n-1/2} + f_0 w_{n+1/2}\phi_{n+1/2} + [f_0\frac{H_n}{H_n+H_{n+1}} w_{n+1/2}(\phi_n-\phi_{n+1}) + f_0\frac{H_n}{H_n+H_{n-1}} w_{n-1/2}(\phi_{n-1}-\phi_n)] \quad (10)$$

The potential energy equation is derived in a similar fashion. Multiplying (3) by $f_0(\phi_n - \phi_{n+1})$ and rearranging terms, at the $n+1/2$th interface we obtain

$$[\frac{1}{2}\frac{f_0^2}{g'_{n+1/2}}(\phi_n-\phi_{n+1})^2]_t = [\frac{1}{2}\frac{f_0^2}{g'_{n+1/2}}(\phi_n-\phi_{n+1})^2]_x\Psi_{n+1/2\,y} - \frac{f_0^2}{g'_{n+1/2}}(\phi_n-\phi_{n+1})(\Psi_n-\Psi_{n+1})_y\phi_{n+1/2\,x} - f_0 w_{n+1/2}(\phi_n-\phi_{n+1}) \quad (11)$$

In Table 2 we briefly interpret and label symbolically the terms in the energy balances (10) and (11), following for the most part the notation of *Pinardi and Robinson* [1986]. If we consider an integral over a wavelength $2\pi/k$ in x and the width of the channel L in y, several terms in the energy balance taken together integrate to zero (these are denoted with asterisks in Table 2). These terms represent redistribution of energy in the field but do not contribute to the growth of the perturbation.

The remaining terms represent either advective or pressure work processes which reveal interactions between the growing perturbation and either the horizontal or vertical shear of the basic state (Table 2). These terms indicate the relative sizes and characteristic structure of the energy transformations leading to the growth of the perturbation. The spatial patterns of these terms will develop asymmetries. Integration over $2\pi/k$ in x and the channel width L in y provides a box model type summary of energy transformations [e.g., *Haidvogel and Holland*, 1978].

We will later find it convenient to use the following notation for integration and summation operations:

$$< KP_n > = \int_0^L \int_0^{2\pi/k} KP_n\,dxdy\,, \quad (12)$$

$$\{KP\} = \sum_{n=1}^{N} < KP_n >\,, \quad (13a)$$

$$\{AP\} = \sum_{n=1}^{N-1} < AP_{n+1/2} >\,. \quad (13b)$$

4. BASIC STABILITY RESULTS

Before presenting the results of the stability analysis, we consider the relevant necessary conditions for instability given our basic state flow. One of the necessary conditions for the instability of an inviscid, zonal flow $U(y, z)$ is that the potential vorticity gradient must be positive within some subregion of the (y, z) plane and negative in others. We define the quasi-geostrophic potential vorticity of the basic state

$$Q_n = -U_{ny} + \frac{H}{H_n}[F_n(\Psi_n - \Psi_{n+1}) - F_{n-1}(\Psi_{n-1} - \Psi_n)] \quad (14)$$

TABLE 2. Perturbation Energy Equation Terms

Symbol	Physical Meaning	Term
$\hat{K}_{nt}$	time rate of change of kinetic energy	$\frac{1}{2}H_n(\nabla\phi_n\cdot\nabla\phi_n)_t$
$\Delta F^t_{\kappa n}$*	horizontal pressure work divergence involving acceleration	$H_n\nabla\cdot(\phi_n\nabla\phi_{nt})$
KP_n	conversion from basic state K_n to perturbation $\hat{K}_n$	$-H_n\phi_{nx}\phi_{ny}\Psi_{nyy}$
$\Delta_x F_{\kappa n}$*	horizontal advection of kinetic energy	$H_n\Psi_{ny}\frac{1}{2}(\nabla\phi_n\cdot\nabla\phi_n)_x$
$\Delta F^a_{\kappa n}$*	horizontal press. work div. involving momentum transport	$H_n\nabla\cdot[-\phi_n\Psi_{ny}(\nabla\phi_n)_x + \phi_n\phi_{nx}\Psi_{nyy}\hat{j}]$
$\delta\hat{f}_{\kappa n}$	transfer of $\hat{K}_n$ out of layer n into layers $n-1$ and $n+1$	$-f_0 w_{n-1/2}\phi_{n-1/2} + f_0 w_{n+1/2}\phi_{n+1/2}$
$-\hat{b}_n$	conversion from $\hat{A}_{n+1/2}$ and $\hat{A}_{n-1/2}$ to $\hat{K}_n$	$f_0\frac{H_n}{H_n+H_{n+1}} w_{n+1/2}(\phi_n-\phi_{n+1}) + f_0\frac{H_n}{H_n+H_{n-1}} w_{n-1/2}(\phi_{n-1}-\phi_n)$
$\hat{A}_{n+1/2t}$	time rate of change of available potential energy	$[\frac{1}{2}\frac{f_0^2}{g'_{n+1/2}}(\phi_n-\phi_{n+1})^2]_t$
$AP_{n+1/2}$	conversion from basic state $A_{n+1/2}$ to perturbation $\hat{A}_{n+1/2}$	$-\frac{f_0^2}{g'_{n+1/2}}(\phi_n-\phi_{n+1})(\Psi_n-\Psi_{n+1})_y\phi_{n+1/2\,x}$
$\Delta_x F_{An+1/2}$*	horizontal advection of available potential energy	$[\frac{1}{2}\frac{f_0^2}{g'_{n+1/2}}(\phi_n-\phi_{n+1})^2]_x\Psi_{n+1/2\,y}$
$\hat{b}_{n+1/2}$	conversion from $\hat{K}_n$ and $\hat{K}_{n+1}$ to $\hat{A}_{n+1/2}$	$-f_0 w_{n+1/2}(\phi_n-\phi_{n+1})$

*Does not contribute to a net energy conversion when integrated over a wavelength $2\pi/k$ and the width of the channel in y.

The first term on the right-hand side of (14) is the portion of Q_n due to the horizontal shear alone, while the remaining terms of (14) are referred to as the vortex stretching terms. An examination of the potential vorticity and potential vorticity gradient (Q_{ny}) of the basic state (shown for the May 22 jet in Figure 3) indicates ripe possibilities for both barotropic and baroclinic instability processes. The components of Q_n and Q_{ny} due to horizontal shear alone and those due to vortex stretching alone are also plotted in Figure 3. Q_{ny} within each layer changes sign at least twice across the jet, raising the possibility of barotropic instability. Q_{ny} also changes sign along most vertical profiles through the jet, indicative of possible baroclinic instability. The complexity of the structure of Q_{ny} for this mixed instability case with $U(y, z)$ from observations makes prediction of the details of the stability characteristics difficult, prior to actually carrying out the calculation.

We turn now to our primary stability results using the standard six-layer basic state profiles (Figure 2). Equation (9) is solved over a range of values for the wavenumber k. We find both the May 22 and June 12 profiles to be unstable to perturbations across a wide spectrum of along-jet wavelengths (Figure 4). Although the magnitudes of the growth rates (kc_i) differ, the two profiles taken from different locations and at separate times are surprisingly similar in their kc_i versus $2\pi/k$ structure. We note a prominent maximum in kc_i at wavelengths of 260 km for May 22 and 265 km for June 12, with e-folding growth periods of 11 days and 7 days respectively. Local maximums in the kc_i versus $2\pi/k$ curve also occur at about 70, 130, and 180 km. The growth rates diminish gradually for scales larger than the maximum at 260-265 km. The calculations were continued out to a maximum wavelength of 800 km (not shown). The maximum growth rate decreases smoothly for the May 22 case from 0.067 d^{-1} at 400 km to 0.023 d^{-1} at 800 km.

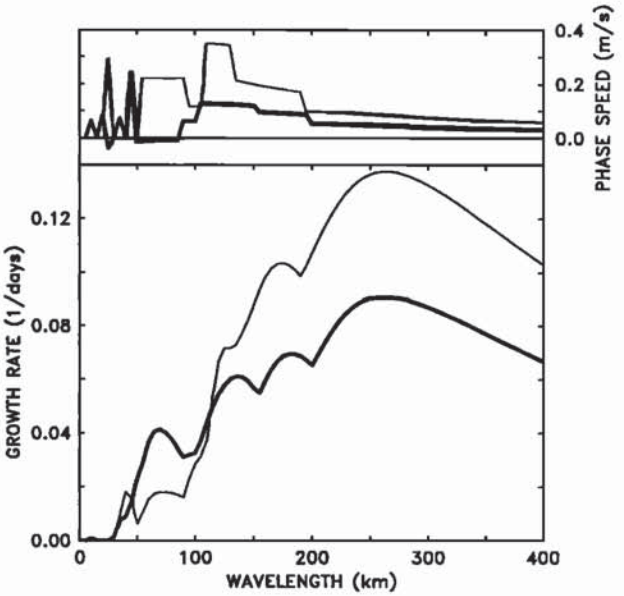

Fig. 4. Phase speeds c_r (top) and growth rates kc_i (bottom) versus along-jet wavelength $2\pi/k$ of the perturbation for the May 22 (bold line) and June 12 (lighter line) cases.

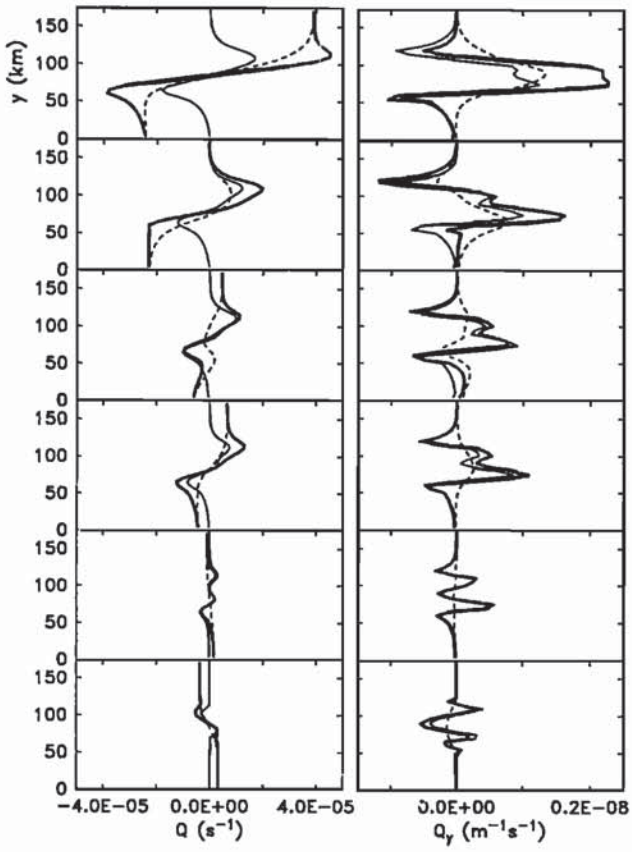

Fig. 3. Potential vorticity Q (left) and potential vorticity gradient Q_y (right) for the May 22 basic state; top panels are for layer 1, second row for layer 2, etc. The bold line is the total Q and Q_y for each layer, the lighter line is the Q and Q_y due solely to the horizontal shear, and the dashed line is the Q and Q_y from the vertical vortex stretching terms.

Growing perturbations propagate with phase speeds c_r which are almost always positive, i.e., downstream (Figure 4). The June 12 case exhibits the largest phase speeds (0.34-0.35 m s^{-1}) between 110 and 130 km wavelengths. The May 22 case has a similar region of maximum phase speed (0.12-0.13 m s^{-1}) from 105-150 km. In general the phase speed results seem organized into distinct regions, with steps between them. These same regions can be identified in the kc_i plots with the local maximums mentioned previously. At the wavelengths corresponding to the most unstable modes for June 12 and May 22 (260-265 km), phase speeds are 0.09 and 0.05 m s^{-1} respectively. With increasing wavelength from this point, c_r gradually decreases. The only substantial region where we see negative phase speeds is from 50 to 85 km in the May 22 case. The June 12 case, however, exhibits moderate positive values (0.22 m s^{-1}) within this same range of wavelengths. Note that all of the phase speed results, both positive and negative, lie within the velocity range of the basic state (Figure 2), as expected. For the reasons stated in section 3, we concentrate on the May 22 profile and present additional results for this case. The June 12 results are similar.

The wavelength $2\pi/k$ for which kc_i is a maximum yields the along-jet scale of the most unstable mode. In this normal mode approximation, the implication is that this mode will probably be the first one to emerge from a background mixture of small-amplitude disturbances. It is plausible, however, that prominent modes other than the most unstable one will be seen as well (see part 2). For this reason we seek to better understand the nature of the instability not only for the growth rate maximum at 260 km but also for large local maxima at 135 and 185 km for the May 22 case. Figure 5 presents kc_i results for the six most unstable

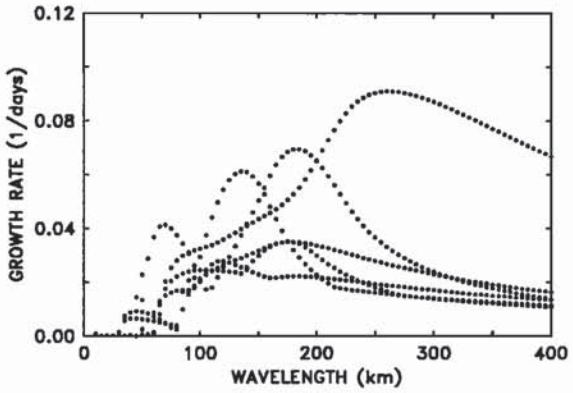

Fig. 5. Growth rates versus along-jet wavelength for the six fastest growing modes at each $2\pi/k$ value, May 22 case.

modes at each $2\pi/k$ value rather than only the most unstable mode. It is apparent that the shape of the kc_i curve in Figure 4 is a result of the superposition of several different growth rate curves which are present throughout a wide range of wavenumbers but take turns in being the most unstable mode. The suspicion that these modes of instability are qualitatively different from one another will be confirmed shortly upon examination of the eigenvector structure.

The solution to the linear stability problem provides no information regarding the actual magnitude of the perturbation velocities. Nevertheless, it is helpful to impose an arbitrary size for a perturbation velocity in order to illustrate the structure of the instability and in anticipation of the move to finite amplitude. For this reason we arbitrarily set a size for the perturbation, choosing the maximum velocity of u_1 in the surface layer perturbation to be 1/3 of the corresponding basic state velocity U_1 at the same y value. The same scaling is used throughout; the relative structure of the perturbation in different parts of the flow is unchanged. This arbitrary scaling of the perturbation will remain constant for all results presented in this study.

The maps of perturbation stream function $\phi_n(x, y)$ (Figure 6*a*) show a characteristic shape where the center of the disturbance is displaced upstream relative to the flanks (termed the "banana" shape by *Holland and Haidvogel* [1980]). This slant of the perturbation streamlines into the horizontal shear of the basic state (Figure 2), giving the impression that it is attempting to decelerate it, is indicative of a barotropic instability process [*Pedlosky*, 1987, section 7.3]. Figure 6*b* shows $\gamma\phi_n(x, y)$ added back into the basic state $\Psi_n(y)$. This presentation is somewhat artificial, since the maps will change depending on how we choose the strength of the perturbation. It is useful, however, to gain some understanding of what form the complete flow field might take and to easily see where the peaks and troughs of the meander occur.

The perturbation vertical velocities $w_{n+1/2}$ (Figure 7*a*) are most intense at the core of the jet, with the largest magnitudes found about halfway between the locations of the crests and troughs in the flow field of Figure 6*b*. The vertical velocities exhibit a characteristic structure that involves positive(negative) $w_{n+1/2}$ for fluid motion from(to) troughs and to(from) crests. This structure of the $w_{n+1/2}$ field is consistent with the form of the perturbation vorticity field $\nabla^2\phi_n$ (Figure 7*b*). The vortex stretching term in equation (2) implies the development of positive vorticity in the troughs of the perturbation and negative vorticity in the crests, as seen in the center of the jet in the perturbation vorticity field. The oppositely signed vorticity at the flanks of the jet reflects perturbations in vorticity associated with growth in amplitude of the unstable wave.

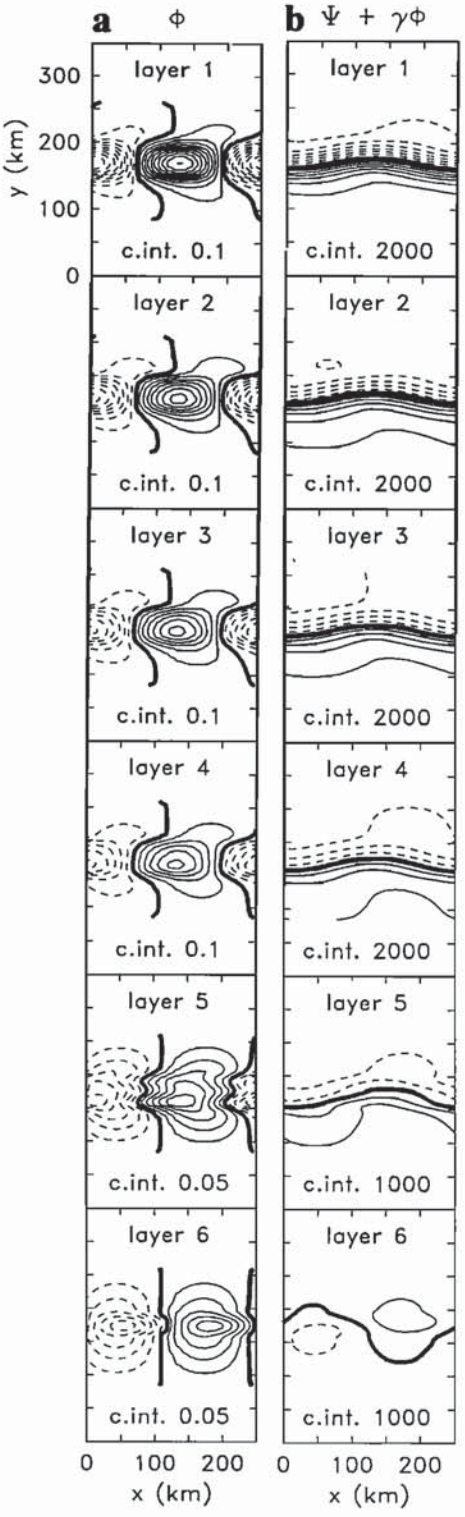

Fig. 6. Maps of (*a*) perturbation stream function and (*b*) basic state + perturbation stream function, for the May 22 case (260 km along-jet wavelength). Solid/bold/dashed lines indicate positive/zero/negative contours.

We also extract vertical sections from our results and plot contours of modal structure (Figure 8) in the (y, z) plane, as *Beckmann* [1988] and others do. This presentation helps clarify the vertical structure of the different modes corresponding to the local

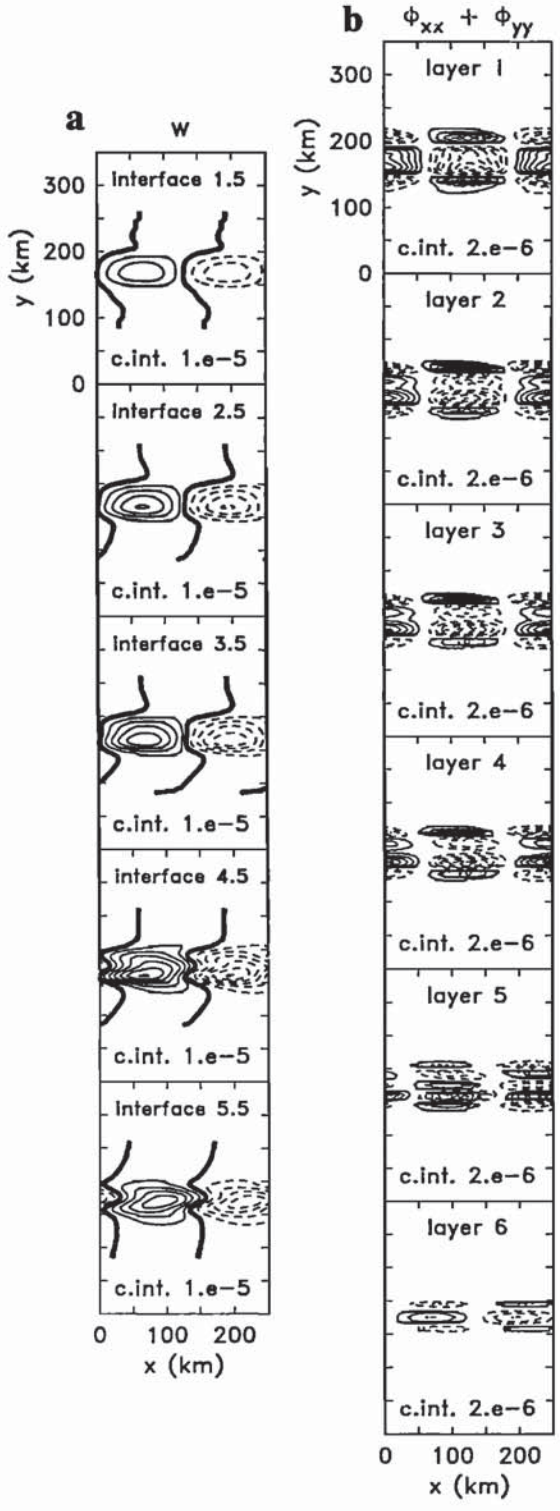

Fig. 7. Maps of (*a*) perturbation vertical velocity *w* and (*b*) perturbation vorticity, for the fastest growing mode from the May 22 case (260 km along-jet wavelength). Solid/bold/dashed lines indicate positive/zero/negative contours.

maxima in kc_i seen at along-jet wavelengths of about 140, 180, and 260 km. We show both the fastest and the second-fastest growing modes at these three wavelengths. Referring to Figure 5, note that the second mode at 180 km appears to be part of the same branch that becomes the first mode at 260 km, and vice-versa. Examination of the structure of the modes at many different wavelengths verifies this crossover. The effect can be seen in Figure 8; mode 1 at 180 km is similar to mode 2 at 260 km, while mode 2 at 180 km is similar to mode 1 at 260 km. The former pair shows a surface-intensified amplitude field while the phase has more depth independence and a maximum value at depth. The latter pair exhibits more depth independence in amplitude. Mode 2 at 140 km and mode 1 at 180 km are also similar. The structure of the phase of mode 1 at 260 km has the largest vertical change of those presented; the perturbation leads from the bottom (also apparent in Figure 7*a*), indicating baroclinic conversion of energy from the basic state to the perturbation.

5. ENERGETICS

Examination of the variation of kc_i with along-jet wavelength and the modal structure of the perturbation does not by itself reveal the balance of energy sources for the mixed instability, although we have noted indications of both barotropic and baroclinic instability processes. We now investigate the relative sizes and structure of these energy transformations. From the development in section 3, we are able to calculate maps of the relevant terms in the kinetic and potential energy balances. The characteristic patterns seen in the maps of the energetics can be usefully compared to similar maps from the nonlinear finite amplitude studies of part 2.

We focus initially on the May 22 case for the wavelength of maximum kc_i (260 km). Figure 9 displays maps of all the terms from the kinetic and potential energy equations which represent net transformations of perturbation energy from one form to another, rather than simply a redistribution of energy within the same field (refer to Table 2). The time rate of change of both perturbation kinetic energy and available potential energy is positive (columns 1 and 2 of Figure 9). The complexity of the structure of $\hat{K}_{nt}$ and $\hat{A}_{n+1/2t}$ is due to the combination of different energy transformation processes taking place, displayed in the remaining five columns of Figure 9.

The term KP_n is the Reynolds stress source term for barotropic instability, representing the cross-jet component of the divergence in the advection of kinetic energy. It contains the perturbation momentum flux $u_n v_n$ which interacts with the horizontal shear of the basic state, yielding a measure of the transformation of basic state kinetic energy (K_n) to perturbation kinetic energy ($\hat{K}_n$). KP_n develops into cross-jet pairs, periodic with x-wavelength half of $2\pi/k$, concentrated where $|U_{ny}|$ is greatest (column 3 of Figure 9). The asymmetries in values of highs and lows, with the high values dominating, indicates a net transformation of K_n to $\hat{K}_n$. A small asymmetry is also apparent in the cross-jet sense; the more intense patterns along the bottom flank of the jet correspond with the asymmetry of the basic state, which has larger horizontal shear on this side. Layers 1 and 4 exhibit the most intense KP_n activity.

The $AP_{n+1/2}$ is the analogous source term for baroclinic instability, indicating the transformation of basic state available potential energy ($A_{n+1/2}$) to perturbation available potential energy ($\hat{A}_{n+1/2}$). $AP_{n+1/2}$ represents the rate of work accomplished by the Reynolds heat flux $(\phi_n - \phi_{n+1})\phi_{n+1/2\,x}$ against the cross-jet gradient of basic state density. $AP_{n+1/2}$ (column 4 of Figure 9) is centered along the jet axis where the basic state vertical shear is greatest. The asymmetries which develop imply a net conversion of $A_{n+1/2}$ to $\hat{A}_{n+1/2}$. The asymmetries and thus conversions at interfaces 1.5 and 4.5 are particularly strong.

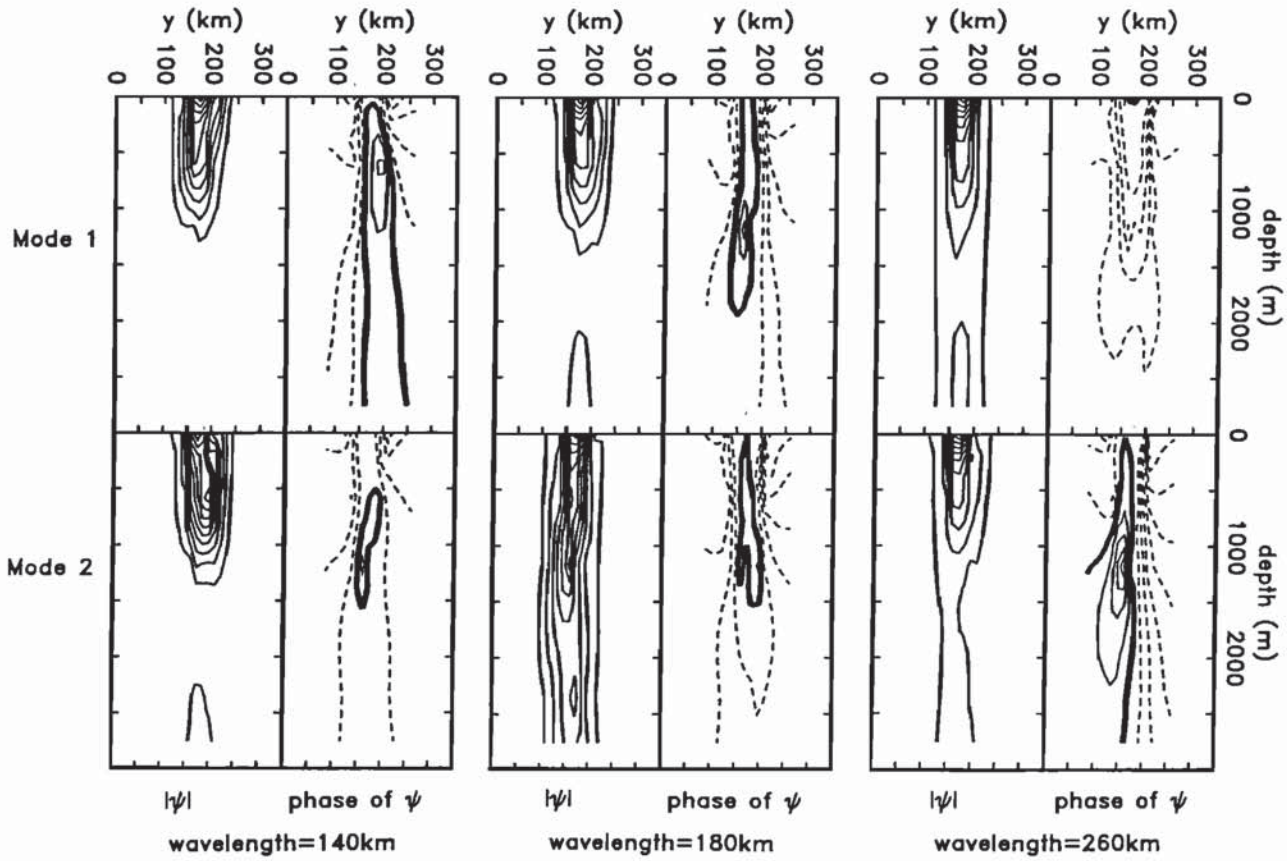

Fig. 8. Vertical sections of perturbation stream function amplitude and phase at three selected along-jet wavelengths, showing the modal structure of the two fastest growing modes, all for the May 22 case. Contour interval for amplitude plots is arbitrary but does not change. Contour interval for phase plots is 15° (solid/bold/dashed lines indicate positive/zero/negative contours).

Columns 5 and 6 of Figure 9 present two views of the buoyancy work energy flux. This is the conversion process internal to the perturbation which allows its kinetic energy to increase at the expense of its available potential energy, or vice-versa. The $\hat{b}_{n+1/2}$ fields at interfaces 4.5 and 5.5 indicate the largest amounts of $\hat{A}_{n+1/2}$ being lost to $\hat{K}_n$. The maps of $-\hat{b}_n$ in turn indicate that layers 4, 5, and 6 are the beneficiaries of the largest amounts of $\hat{K}_n$ from this conversion process. The patterns of buoyancy work seem to exhibit a less symmetrical cross-jet structure among the lower layers as opposed to the upper ones.

The rightmost column of Figure 9 maps the vertical pressure work term $\delta\hat{f}_{\pi n}$. This represents the conversion of $\hat{K}_n$ from one layer to another. The patterns of $\delta\hat{f}_{\pi n}$ are periodic at half of $2\pi/k$ rather than a full wavelength. Layer 1 exhibits the most intense highs and lows, although it is not clear that much net transfer in or out of layer 1 occurs.

By integrating each of these terms across the channel and over a perturbation wavelength $2\pi/k$, we obtain a sense of the overall importance of different energy transformations. The absolute values of the resulting numbers will have no meaning but their relative sizes provide a convenient summary of the relative importance of the different energy transformations. Figures 10*a*-10*c* follow in the tradition dating back to *Phillips* [1956] in presenting a box model view of the integrated energy fluxes $< KP_n >$, $< AP_{n+1/2} >$, $< \hat{b}_{n+1/2} >$, and $< \delta\hat{f}_{\pi n} >$. The values are arbitrarily normalized such that the conversion $KP_1 = 1.00$. The thickness of an arrow is proportional to the indicated energy transfer. Capital letters inside rectangles are used to represent the basic state, while lowercase letters within ovals symbolize the perturbation.

The energy summary for the maximum growth rate (Figure 10*c*), confirms at a glance what we have already guessed at; both barotropic and baroclinic energy transformations are important to the growth of the perturbation. Figure 10*c* provides a synopsis of the same information contained in Figure 9. Both the $< KP_n >$ and the $< AP_{n+1/2} >$ terms are feeding the perturbation at all levels. The dominant transfers are from the mean to perturbation kinetic energy in layers 1 and 4 and the mean to perturbation potential energy at interfaces 4.5 and 5.5; the other energy fluxes are insignificant.

From the kc_i versus wavelength characteristics (Figures 4 and 5), the phase speed behavior (Figure 4), as well as the modal structure (Figure 8), it appears as if the local growth rate maximums observed at about 130 and 180 km are associated with perturbations that are distinct features, different in nature from those at 260 km. We present the global energetics at 130 and 180 km in Figures 10*a* and 10*b*, and the qualitative differences between these features are again clear.

At 130 km (Figure 10*a*), the barotropic instability processes are dominant, especially within layers 1 and 4. Interestingly, the potential energy of the perturbation is actually flowing in the "wrong" sense, back into the mean. *Haidvogel and Holland* [1978] also present such a case in one of their linear stability analyses. They suggest that as the perturbation grows to finite amplitude, the sign of this transfer will change back to the "right" direction (also discussed by *Veronis* [1981]). Finite amplitude results

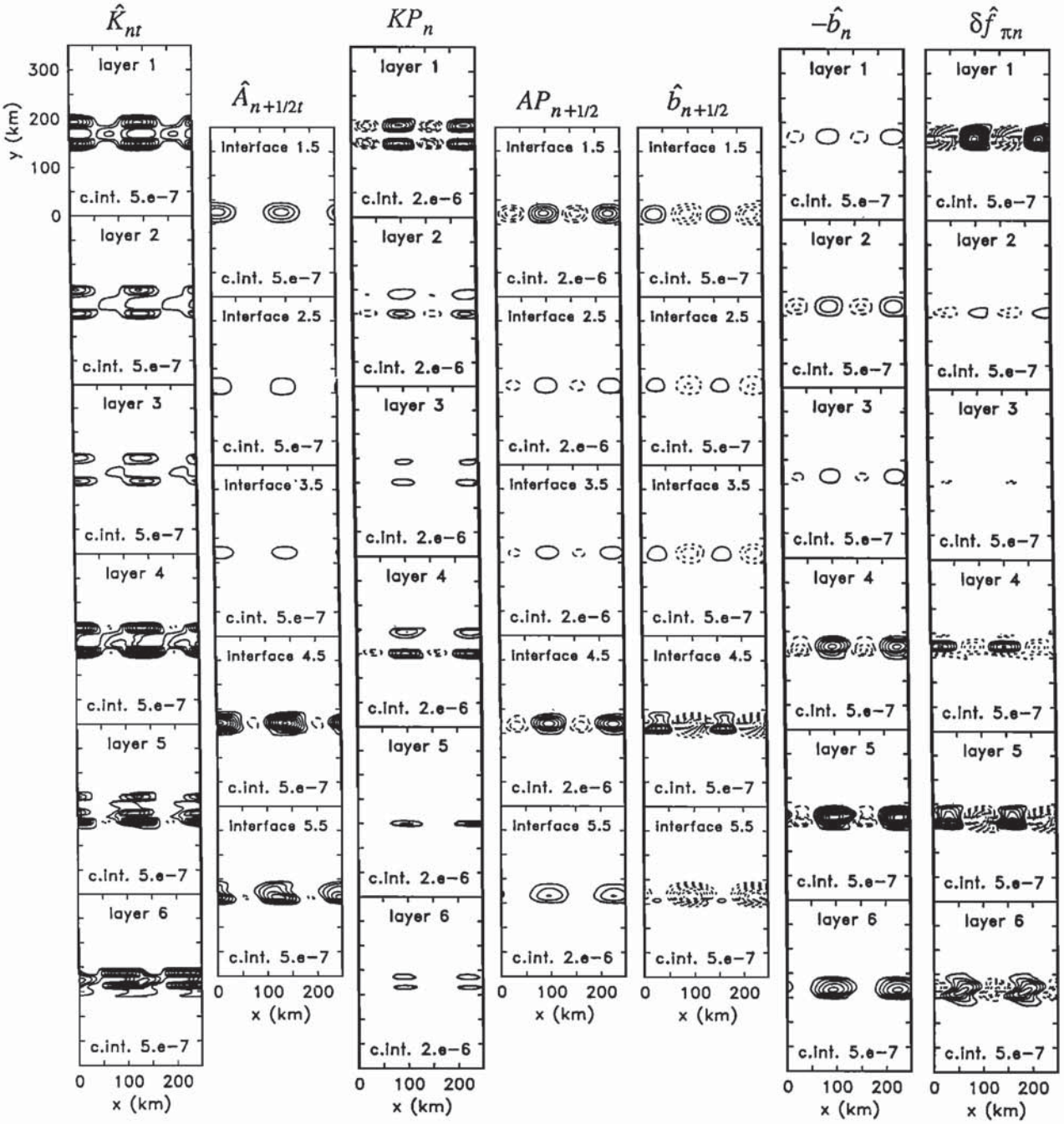

Fig. 9. Maps of the energy transformation terms (see text and Table 2 for definitions) for the 260-km along-jet wavelength May 22 case (solid/bold/dashed lines indicate positive/zero/negative contours).

involving this behavior are found in part 2. The other notable feature of the global energetics at 130 km is the tendency for kinetic energy in the perturbation to be transferred down into the lower layers through the $< \delta \hat{f}_{\pi n} >$ terms, especially within layers 1-4. Much of the energy coming from the KP_1 process is actually flowing down the water column and supplying lower layers.

At 180 km (Figure 10*b*), barotropic instability processes are still dominant within layers 1 and 4. The conversion in layer 4 is now the largest, rather than that in layer 1. The baroclinic processes are nearly neutral, contributing little in either sense. The vertical transfer of kinetic energy downward via $< \delta \hat{f}_{\pi n} >$ is even stronger in this case than at 130 km.

As a measure of the overall volume-integrated importance of baroclinic versus barotropic instability processes for the perturbation we consider the ratio $\{AP\}/\{KP\}$, using the notation of (13). Figure 11 shows the ratio $\{AP\}/\{KP\}$ over the range of alongjet wavelengths. For wavelengths less than ≈90 km, the instabilities are almost entirely barotropic in nature. From ≈110-190 km, barotropic instability processes still dominate; the negative values of $\{AP\}/\{KP\}$ are due to $\{AP\} < 0$ and $\{KP\} > 0$. The flow of potential energy is from perturbation to mean, but the barotropic conversion process is large enough to maintain the instability. Both the 130 and 180-km cases discussed previously fall into this category.

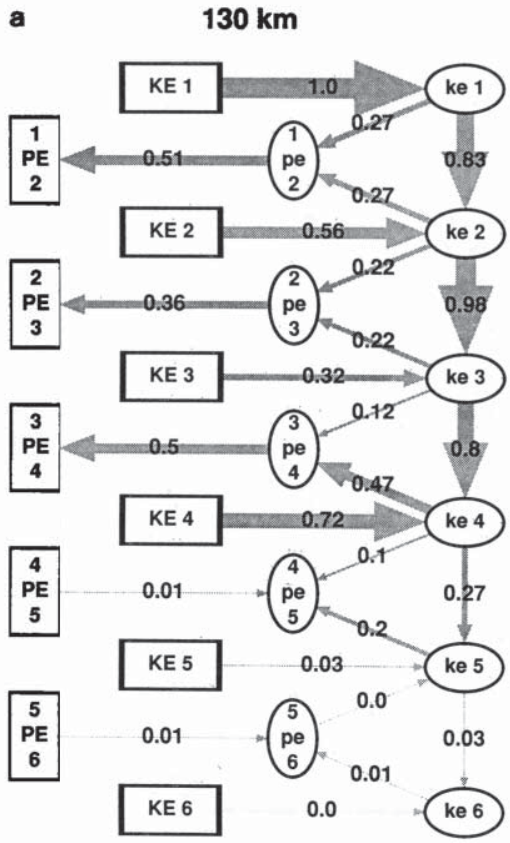

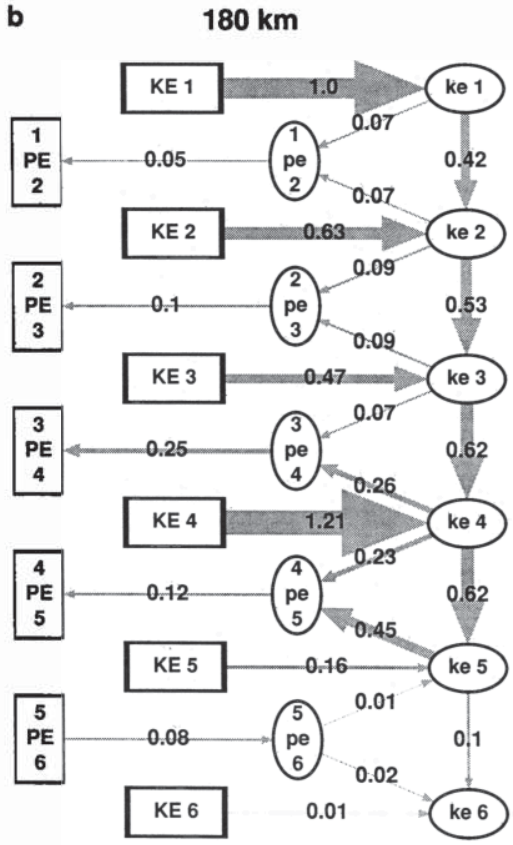

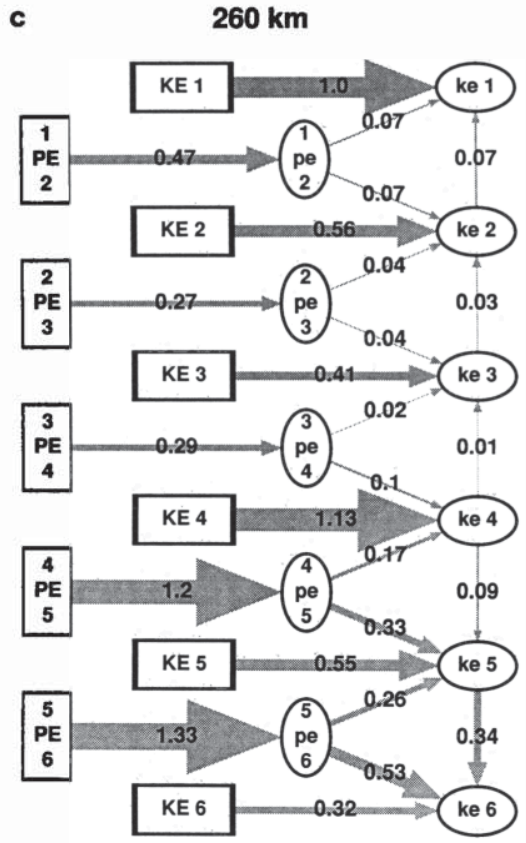

Fig. 10. Graphical presentation of the integrated energy fluxes at (*a*) 130 km, (*b*) 180 km, and (*c*) 260 km along-jet wavelength ($2\pi/k$) for May 22 case. The thickness of the shaft of an arrow is proportional to the relative size of the indicated energy transfer, which is also given a numerical value. The energy fluxes are normalized such that the transformation of basic state kinetic energy to perturbation kinetic energy in layer 1 is 1.00. Capital labels inside rectangles symbolize the basic state; lowercase labels inside ovals symbolize the perturbation.

With wavelength increasing from ≈200 km, both baroclinic and barotropic instability processes contribute significantly to the growth of the perturbation. A gradual tendency toward a more baroclinic instability occurs with increasing wavelength. The most unstable mode (at 260 km) is characterized by $\{AP\}/\{KP\} = 0.90$. Thus baroclinic and barotropic instability

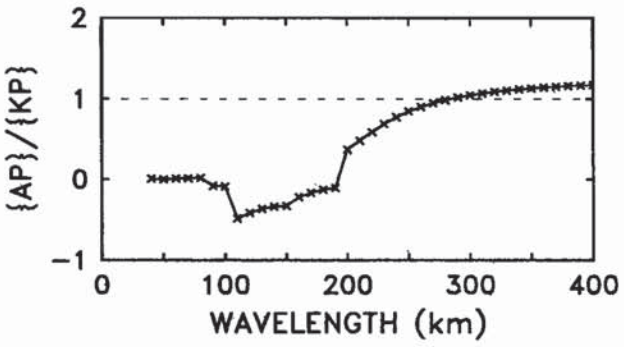

Fig. 11. The ratio of the relative importance of baroclinic/barotropic instability processes ($\{AP\}/\{KP\}$) for the standard May 22 case, as a function of along-jet wavelength. Negative values of $\{AP\}/\{KP\}$ are due to $\{AP\} < 0$ (energy flow from perturbation to mean) and $\{KP\} > 0$.

processes are of nearly equal importance for the fastest growing mode.

6. VARIATIONS

Increased Vertical Resolution

One of the points made by *Beckmann* [1988] as well as others is the importance of using sufficient layers in the vertical to avoid the well-known short-wavelength cutoff often noted in idealized studies. This effect is seen, for example, among the two-layer idealized jet linear stability results of *Holland and Haidvogel* [1980]; their growth rates go rapidly to zero with decreasing wavelength from about 200 km. *Walstad et al.* [this issue] investigate the use of a 12-layer model and conclude that the six-layer model is sufficient for this region. We test the use of the same 12-layer model, which is equivalent to our six-layer May 22 basic case (Figure 2*b*) except for the increased vertical resolution. The 12-layer basic state is described in Table 3 and Figure 12*b*. In addition, we create a nine-layer equivalent case by combining the bottom six layers of the 12-layer model into three layers. The nine-layer basic state is described by Table 4 and Figure 12*a*.

The growth rates and phase speeds for the equivalent six, nine, and 12 layer models are quite similar (Figure 13). The kc_i maximum for the 12-layer case now occurs at 250 km rather than 260 km for the six-layer case. The nine-layer case splits the difference between them fairly neatly. From roughly 170 to 250 km, notice that with decreasing numbers of layers, the kc_i curve shifts slightly to the right. This is the extent of the short-wavelength cutoff phenomenon in this case, and the differences are minor. In the 12-layer case, the local maximum in growth rate at ≈180 km is no longer present, but the magnitude of the growth rate here is comparable to the six-layer case. The differences among the curves for $2\pi/k < 170$ km are not too substantial but more diffi-

TABLE 3. Nine-Layer Basic State Characteristics

Layer	Thickness, m	$g\Delta\rho/\rho_0$, m s^{-2}
1 (surface)	48	
		6.0443×10^{-3}
2	60	
		7.0874×10^{-3}
3	84	
		3.2294×10^{-3}
4	102	
		2.0391×10^{-3}
5	138	
		2.0421×10^{-3}
6	176	
		3.0625×10^{-3}
7	528	
		3.2539×10^{-3}
8	896	
		2.5541×10^{-3}
9 (bottom)	1138	

TABLE 4. Twelve-Layer Basic State Characteristics

Layer	Thickness, m	$g\Delta\rho/\rho_0$, m s^{-2}
1 (surface)	48	
		6.0443×10^{-3}
2	60	
		7.0874×10^{-3}
3	84	
		3.2294×10^{-3}
4	102	
		2.0391×10^{-3}
5	138	
		2.0422×10^{-3}
6	176	
		2.0965×10^{-3}
7	232	
		1.7234×10^{-3}
8	296	
		1.6041×10^{-3}
9	392	
		1.5863×10^{-3}
10	504	
		1.3437×10^{-3}
11	572	
		1.0390×10^{-3}
12 (bottom)	566	

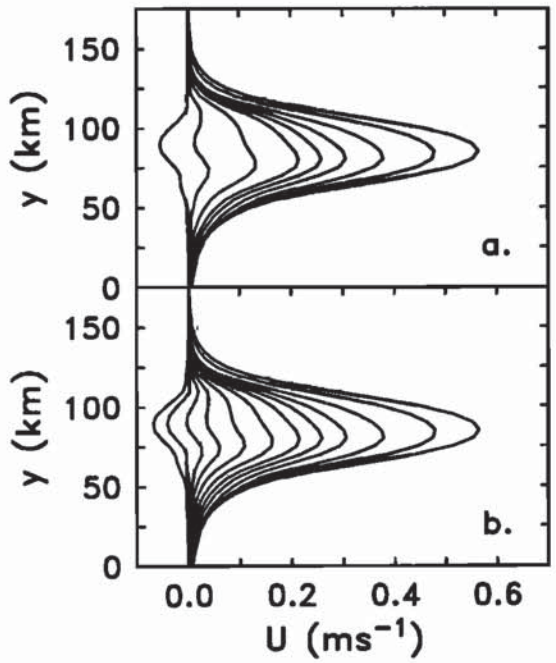

Fig. 12. Basic state profiles for the (*a*) nine-layer case and (*b*) 12-layer case, both from May 22.

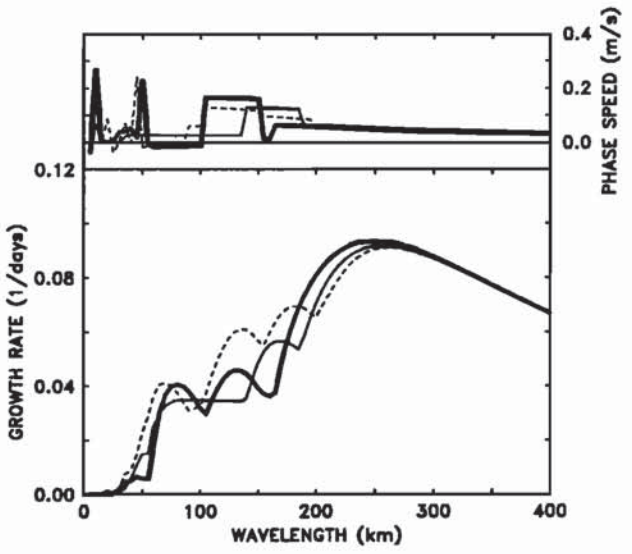

Fig. 13. Phase speeds and growth rates for the 12-layer case (bold line), nine-layer case (normal line), and standard six-layer case (dashed line), all from May 22.

cult to interpret. In the 130-km region, the 12-layer local maximum in kc_i is about 30% smaller than the six-layer case. The three curves converge again with decreasing wavelength from this point. For simplicity and for consistency with *Walstad et al.* [this issue] and part 2, we use the six-layer model for our primary results and interpretation.

One-Dimensional Cases

As another approach to the question of the importance of barotropic versus baroclinic processes in this region, we thought it would be instructive to investigate the corresponding one-dimensional cases. We create a pure baroclinic model, with strictly vertical shear, by averaging the May 22 horizontal jet profile over y while retaining the same layer structure in the vertical (resulting velocity profile listed in Table 5). Similarly, we create a pure barotropic case, with only horizontal shear, by averaging (weighted by layer thickness) all six layers vertically into a single layer model (Figure 14). The asymmetry of the basic state (which has always been present) is particularly evident in Figure 14. The stability analysis is accomplished using almost exactly the same methods as previously outlined, with straightforward simplifications of the formulas.

The results (Figure 15) are satisfying in that they offer additional clues as to the structure of the mixed stability case. The pure barotropic case exhibits a kc_i maximum at 110 km, while the pure baroclinic has maximum kc_i at 285 km. Results for c_r are similar for all cases except for a 105-195 km region where the mixed case perturbation propagates roughly twice as fast as the others. For wavelengths smaller than ≈170 km, the pure barotropic and the fully mixed cases are similar, although the mixed case is usually more unstable. For wavelengths larger than ≈170 km, the pure baroclinic results are close to the mixed ones, although less unstable for shorter wavelengths and more unstable for longer ones. The mixed case is substantially more unstable than the pure barotropic one at larger wavelengths. These results are consistent with some findings of *Song* [1971], who performs similar comparisons for a variety of idealized situations. From the point of view of a barotropic jet, the addition of vertical shear tends to destabilize at all wavelengths. If horizontal shear is added to a pure baroclinic problem, on the other hand, it has a destabilizing effect for shorter wavelengths but a stabilizing effect at longer ones. Note, in general, that the multiple peaks in growth rate seen in the mixed stability case are not present in the one-dimensional cases; the complexity of the mixed case is evidently related to the combination of different instability mechanisms occurring simultaneously.

TABLE 5. Pure Baroclinic Model

Layer	Basic State Velocities, m s^{-1}
1 (surface)	0.24
2	0.17
3	0.14
4	0.10
5	0.04
6 (bottom)	-0.01

Layer thicknesses and g' values are listed in Table 1.

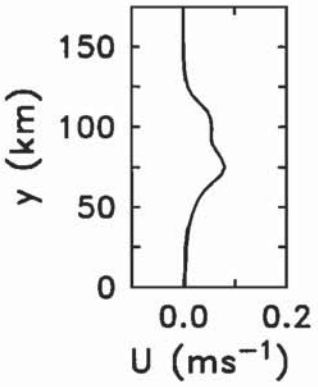

Fig. 14. Basic state profile for the May 22 pure barotropic, single-layer case.

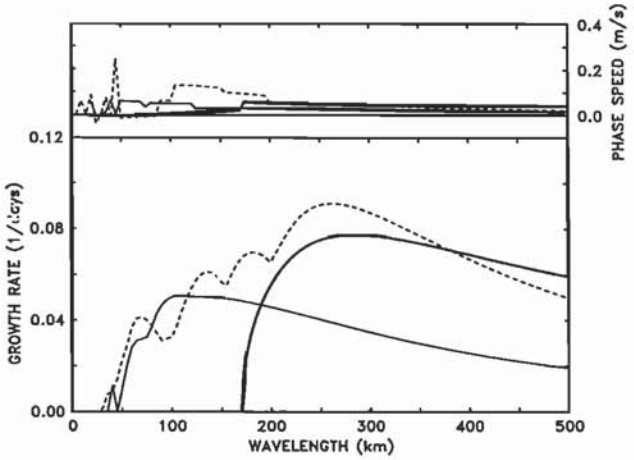

Fig. 15. Phase speeds and growth rates for the pure baroclinic instability case (bold line), the pure barotropic instability case (normal line), and the standard six-layer mixed instability case (dashed line), all from May 22.

The one-dimensional results are consistent with our analysis of the energetics of the mixed case (section 5). We found that the instability at 260 km was characterized by nearly equal contributions from barotropic and baroclinic processes. Figure 15 indicates that purely barotropic and baroclinic instability mechanisms produce roughly comparable growth rates. The dominance of barotropic energy transformations around the secondary maximum at 180 km (Figure 11) also agrees with these results, since at this wavelength the pure baroclinic case has very small kc_i. The pure baroclinic case illustrates well the cutoff at short wavelengths mentioned above. In Figure 15, the increasing relative importance of baroclinic processes as we move to longer wavelengths is also consistent with the energy analysis of the mixed case; at 260 km the $\{AP\}/\{KP\}$ ratio from the global energetics is 0.90, while at 400 km this ratio has increased to 1.18 (Figure 11).

Nonzonal Cases and the Beta Effect

The linear stability model was developed on an f plane, for simplicity and also for consistency with part 2 of the study. We calculate for layer 1 the dimensionless parameter $\beta^* = \beta L^2 U_0^{-1} \approx 0.029$ ($\beta = 1.8 \times 10^{-11}$ m^{-1} s^{-1}, $U_0 = 0.53$ m s^{-1}, $L = 29$ km), which is small, so the beta effect is probably minor. For this type of analysis, however, the extension to the beta plane and to arbitrary basic state orientation (for the two-dimensional parallel mean flow which we consider here) turns out to be straightforward numerically [*Robinson and McWilliams*, 1974].

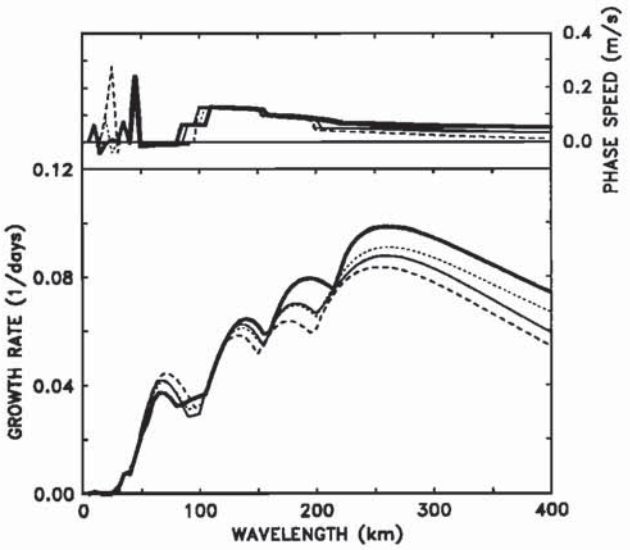

Fig. 16. Phase speeds and growth rates for the May 22 case with the beta effect for a westward flowing jet (bold line), eastward flowing jet (big dashes), and southward flowing jet (normal line), compared to the standard f plane case (small dashes).

While maintaining the coordinate system aligned with the mean state orientation, we now define both a $\beta^{(x)} = f_x$ and a $\beta^{(y)} = f_y$. Adding these terms to our development, (8) now takes the form (dimensional)

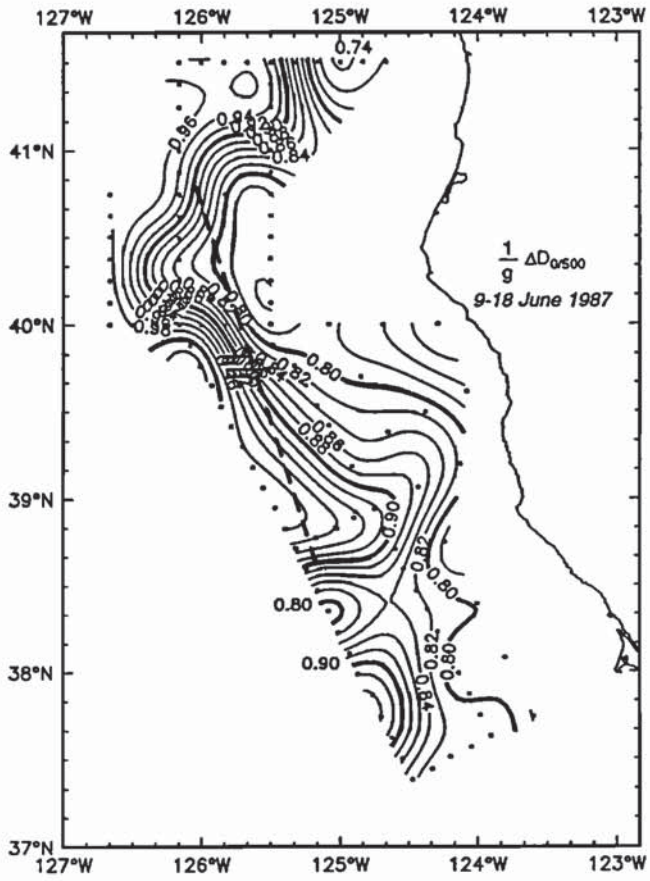

Fig. 17. $\Delta D_{0/500}/g$ (m), the dynamic height of the sea surface relative to 500 dbars, normalized by g, over the complete survey grid for the 1987 summer cruise [*Kosro et al.*, this issue]. The dashed line is drawn to help make a rough estimate of a meander wavelength, which is ≈250 km.

$$(U_n - c)\{\hat{\phi}_{nyy} - k^2\hat{\phi}_n + \frac{H}{H_n}[F_n(\hat{\phi}_{n+1} - \hat{\phi}_n) - F_{n-1}(\hat{\phi}_n - \hat{\phi}_{n-1})]\}$$

$$-\hat{\phi}_n\{U_{nyy} - \beta^{(y)} + \frac{H}{H_n}[F_n(U_{n+1} - U_n) - F_{n-1}(U_n - U_{n-1})]\}$$

$$+\frac{i}{k}\hat{\phi}_{ny}\beta^{(x)} = 0\ , \qquad (15)$$

and may be solved as before. The resulting differences in growth rates and phase speeds for our standard May 22 case are shown for three choices of basic state orientation (Figure 16): eastward ($\beta^{(x)}=0$, $\beta^{(y)}=\beta$), equatorward ($\beta^{(x)}=\beta$, $\beta^{(y)}=0$), and westward ($\beta^{(x)}=0$, $\beta^{(y)}=-\beta$), where $\beta = 1.8\times10^{-11}$ m^{-1} s^{-1}. For an equatorward flow, which is the general orientation of the CTZ jet, the most unstable mode has an inverse growth rate of 11.4 days rather than the 11.0 days in the case without the beta effect. The beta effect is slightly stabilizing in all cases except for a westward tending mean flow, where it is slightly destabilizing. If we choose a mean flow aimed directly to the west, the inverse growth rate of the most unstable wave is 10.0 days rather than the 11.0 days of the case without the beta effect. The results for all of the cases in Figure 16 are qualitatively similar. We conclude that the beta effect has a relatively minor influence on the linear stability of the jet profiles.

7. SUMMARY

We take advantage of the combined hydrographic and ADCP data from the 1987 CTZ experiment to perform a quasi-geostrophic linear stability analysis of a CTZ jet using observed profiles. The basic state flow fields are somewhat idealized, but they retain much of the complexity of the real ocean and yield richly structured results. We primarily apply well-tested linear stability analysis techniques to the coastal transition zone region. Additional motivation for the linear analysis is to provide necessary information for the finite amplitude nonlinear study in part 2.

We treat the fully mixed linear stability problem (with both horizontal and vertical shear), with relatively fine resolution in both y and z, using basic state profiles from objectively analyzed data. We examine the behavior of the growth rates, phase speeds, and eigenvector structure as a function of along-jet wavelength. We also analyze the energetics to determine the degree to which baroclinic and barotropic instability processes are important and the structure of the energy transfers. The application of similar techniques to the extensive 1988 CTZ data set is currently being explored.

One of our major results is the identification of the fastest growing instability with an along-jet wavelength of ≈260 km. The characteristic inverse growth rate of this meander is 7-11 days, and the propagation speed of the perturbation is 0.05-0.09 m s^{-1} downstream, using the differences between our May 22 and June 12 results as a measure of uncertainty. The comparison of these results to actual meanders seen in either modeling or observations will always be problematic; the linearized theory is only valid for infinitesimally small-amplitude perturbations. It is remarkable how fruitful the linear theory has been, however, and even mature fluctuations will often be approximately explained well past the formal limits of the theory [*Pedlosky*, 1987, section 7.3].

With the preceding caveat, then, consider the flow field of Figure 17 from *Kosro et al.* [this issue]. This is the complete June survey dynamic height field. We only considered the southern half of the array previously (see Figure 1), following *Walstad et al.* [this issue]. A look now at the full survey reveals a large meander extending from about 38°40′N to 41°N. Although irreg-

ular in shape, the length of this feature is still fairly well defined. If we consider the $\Delta D = 0.9$ contour and draw a straight line such that the line is bisected by the contour, we obtain a rough estimate of 250 ± 20 km for the wavelength. The persistent maximum seen at a wavelength of ≈260 km throughout our linear stability results is consistent with the size of this observed meander.

The phase speed results of the model imply a 4-8 km/d propagation of a perturbation downstream. This propagation of the jet meander is difficult to identify even qualitatively from the observations, given the available data and the complexity of the flow field. In the northern region of the 1987 CTZ experiment, off of Cape Mendocino, phase propagation is not clearly evident (see e.g., *Kosro et al.* [this issue]). In the southern region of the *Walstad et al.* [this issue] grid (south of about 38° N, our Figure 1), the jet features do appear to translate roughly 50 km downstream from May 22 to June 12. The linear stability results predict a larger shift of 80-160 km over this same time period. The results from part 2, however, indicate that the propagation velocities of finite amplitude meanders are, in fact, generally smaller than the linear stability values.

Finally, our analysis of the energetics of the meander growth verifies that the instability is a mixed one, with conversions from both the basic state kinetic energy and basic state potential energy. We go on to provide detailed energy balance information. The primary result is that unstable solutions over a range of wavelengths from 200 to 400 km are all characterized by substantial contributions from both barotropic and baroclinic instability processes, and these two sources of energy are of nearly equal importance for the fastest growing fluctuation.

Acknowledgments. S.D.P. was supported by Office of Naval Research (ONR) Coastal Sciences grant N00014-90-J-1211, ONR Mesoscale Physical Oceanography grant N00014-90-J-1177, and National Science Foundation grant OCE-8709930. J.S.A. and L.J.W. were supported by ONR Coastal Sciences grants N00014-90-J-1051 and N00014-87-K-0009. Thanks to Priscilla Newberger for assistance with the basic state profiles and to P. M. Kosro and A. Huyer for the high quality of the data. S.D.P. thanks Robert L. Smith for support and encouragement during this study.

REFERENCES

Allen, J. S., L. J. Walstad, and P. A. Newberger, Dynamics of the coastal transition zone jet, 2, nonlinear finite amplitude behavior, *J. Geophys. Res.*, this issue.

Beckmann, A., Vertical structure of midlatitude mesoscale instabilities, *J. Phys. Oceanogr., 18,* 1354-1371, 1988.

Coastal Transition Zone Group, The Coastal Transition Zone Program, *Eos Trans. AGU, 69,* 698-699,704,707, 1988.

Haidvogel, D. B., and W. R. Holland, The stability of ocean currents in eddy-resolving general circulation models, *J. Phys. Oceanogr., 8,* 393-413, 1978.

Hart, J. E., On the mixed stability problem for quasi-geostrophic ocean currents, *J. Phys. Oceanogr., 4,* 349-356, 1974.

Holland, W. R., and D. B. Haidvogel, A parameter study of the mixed instability of idealized ocean currents, *Dyn. Atmos. Oceans, 4,* 185-215, 1980.

Huyer, A., et al., Currents and water masses of the coastal transition zone off northern California, June to August 1988, *J. Geophys. Res.*, this issue.

Johns, W. E., One-dimensional baroclinically unstable waves on the Gulf Stream potential vorticity gradient near Cape Hatteras, *Dyn. Atmos. Oceans, 11,* 323-350, 1988.

Kaufman, L. C., The LZ algorithm to solve the generalized eigenvalue problem for complex matrices, *ACM Trans. Math. Software, 1,* 271-281, 1975.

Killworth, P. D., Barotropic and baroclinic instability in rotating stratified fluids, *Dyn. Atmos. Oceans, 4,* 143-184, 1980.

Kosro, P. M., et al., The structure of the transition zone between coastal waters and the open ocean off northern California, winter and spring 1987, *J. Geophys. Res.*, this issue.

Pedlosky, J., *Geophysical Fluid Dynamics,* 710 pp., Springer-Verlag, New York, 1987.

Phillips, N. A., The general circulation of the atmosphere: a numerical experiment, *Q. J. R. Meteorol. Soc., 82,* 123-164, 1956.

Pinardi, N., and A. R. Robinson, Quasigeostrophic energetics of open ocean regions, *Dyn. Atmos. Oceans, 10,* 185-219, 1986.

Robinson, A. R., and J. C. McWilliams, The baroclinic instability of the open ocean, *J. Phys. Oceanogr., 4,* 281-294, 1974.

Song, R. T., A numerical study of the three-dimensional structure and energetics of unstable disturbances in zonal currents: part II, *J. Atmos. Sci., 28,* 565-586, 1971.

Strub, P. T., et al., The nature of the cold filaments in the California current system, *J. Geophys. Res.*, this issue.

Veronis, G., Dynamics of large-scale ocean circulation, in *Evolution of Physical Oceanography,* edited by B. A. Warren and C. Wunsch, pp. 140-183, M.I.T. Press, Cambridge, Mass., 1981.

Walstad, L. J., J. S. Allen, P. M. Kosro, and A. Huyer, Dynamics of the coastal transition zone in 1987 through data assimilation studies, *J. Geophys. Res.*, this issue.

J. S. Allen, S. D. Pierce, and L. J. Walstad, College of Oceanography, Oregon State University, Oceanography Admin. Bldg. 104, Corvallis, OR 97331-5503.

(Received January 14, 1991;
accepted March 21, 1991.)